Research Square

Preprints are preliminary reports that have not undergone peer review.
They should not be considered conclusive, used to inform clinical practice,
or referenced by the media as validated information.

Durability enhancement of ancient masonry via in-situ synthesized silicon- magnesium composite gel: Interfacial chemistry and long-term field monitoring

Tingting Yue

182365937106163.com

Shangqiu University

Jianwei Yue

Henan University

Article

Keywords: Building rehabilitation, Masonry durability, Composite gel, Heritage conservation, Long-term monitoring

Posted Date: November 26th, 2026

DOI: https://doi.org/10.21203/rs.3.rs-11779060/v1

License: This work is licensed under a Creative Commons Attribution 4.0 International License.
Read Full License

Additional Declarations: No competing interests reported.

Durability enhancement of ancient masonry via in-situ synthesized silicon-magnesium composite gel: Interfacial chemistry and long-term field monitoring

Tingting Yue[a,b]* , Jianwei Yue[c]

[a] *School of Landscape Architecture and Architecture, Shangqiu University. Shangqiu 476000, China.*

[b] *Tianjin University School of Civil Engineering, Tianjin University, Tianjin 300072, China.*

[c] *School of Architectural Engineering, Henan University. Kaifeng 475004, China.*

Abstract

Repeated drying-wetting and freeze-thaw cycles severely deteriorate ancient masonry structures, threatening the long-term conservation of architectural heritage. Addressing this, a novel silicon-magnesium composite gel was developed for the deep rehabilitation of historic gray bricks via in-situ copolymerization and vacuum-assisted pressure infiltration. The chemical evolution and structural stability of the composite network were systematically characterized using FTIR, XRD, and XRF, which confirmed the formation of stable covalent bonds (Si-O-Mg and Si-O-C) bridging the organic and inorganic phases. Orthogonal experimental design optimized the formulation, yielding a practical operable curing time (5.33–6.41 h) suitable for deep penetration. SEM observations revealed a continuous interpenetrating network that effectively filled microcracks and connected pores, significantly densifying the matrix. Uniaxial compression tests demonstrated a substantial improvement in the mechanical integrity of the modified bricks. Furthermore, an outdoor experimental wall was constructed for long-term durability monitoring. Moisture sensor data and infrared thermal imaging after rainfall verified that the treated wall exhibited substantially reduced internal moisture content, inhibited capillary water rise, and dampened diurnal temperature fluctuations compared to the untreated control. This work provides a sustainable and extensible reinforcement strategy for the engineering conservation of ancient masonry buildings.

Keywords: Building rehabilitation; Masonry durability; Composite gel; Heritage conservation; Long-term monit oring

1.Introduction

As the carriers of historical memory, brick and stone relics embody profound cultural connotations and historical value, but they bear complex threats from environmental changes [1-2]. This type of immovable heritage is dominated by natural porous materials such as sintered bricks, sandstones, and limestones. Its physical structure and chemical properties are not only storage media for historical information, but also complex systems that need to be cracked by contemporary protection technologies [3-5]. The characteristics of open-air preservation make it exposed to natural pressures such as temperature and humidity fluctuations, acid rain erosion, and biodegradation for a long time, and the huge volume and immobility limit the implementation of active protection methods [6-11]. The high pore structure of the masonry material forms a capillary channel to promote the continuous invasion of water and dissolved salts into the interior [12], causing chemical erosion such as salt crystallization expansion, alkaline substance migration, and weakening the binding force between particles, resulting in material alkalization and layered spalling [13-18] (as shown in Fig. 1, typical deterioration of the Kaifeng city wall and Luoyang Longmen Grottoes includes cracking, erosion, laminar spalling, and weathering). The cyclic process of dry-wet

* Corresponding author at: Tianjin University School of Civil Engineering. Tianjin.
E-mail address: 18236593710@163.com

alternation further amplifies the damage to pore structure, promotes the expansion of micro-cracks into macro-cracks, and the mechanical strength declines exponentially [19-20]. How to construct a blocking mechanism for water migration path and slow down the vicious interaction between material and environment has become the core proposition to balance the protection needs of cultural relics and the law of natural decay [21].

In recent years, the research on water migration inhibition in the field of architectural heritage protection has mainly focused on two directions: external and groundwater isolation measures, and hydrophobic treatment technology of wall surface based on chemical modification. With the breakthrough of material chemistry and the urgent need for cultural heritage protection, the research on wall-modified materials with both waterproof performance and historical compatibility is becoming the focus of academic circles. Current research especially emphasizes the development of new composite materials through molecular engineering methods, aiming to achieve lasting moisture-proof effects while maintaining the physical and chemical integrity of traditional building substrates. Guo [22] used the alcohol solution of barium hydroxide as a consolidation agent for weathering brick masonry, and the results showed that it played a role in filling and bonding weathered pores and cracks. Bu [23] et al.prepared a fluorine-containing B72 hybrid methyl-modified silica / (Ag-doped TiO_2) hexamethyldiazepine hybrid (HMDS) H-SiO_2 / Ag / TiO_2) superhydrophobic organic-inorganic composite coating by a mild and environmentally friendly method. Reyes-Tesillo [24] developed a nano-satellite coating made of polymethyl methacrylate and SiO_2-TiO_2 particles (PMMA / SiO_2-TiO_2), and evaluated its high vacuum resistance by quantifying its weight loss. Graziani [25] applied TiO2-based photocatalytic nano-coating to ancient bricks, and photocatalytic nano-coating can effectively inhibit biological scaling on the surface of bricks. Pagliolico [26] et al.prepared a nano-composite film by combining a waterborne acrylic resin curing process with in-situ nano-silica heat treatment with alkoxysilane as a precursor.

The weathering surface of brick and stone cultural relics has typical characteristics such as high porosity, strong water absorption, and weakened mechanical properties. As an inorganic-organic hybrid material, tetraethoxysilane (TEOS) is widely used in the reinforcement and protection of masonry relics due to its excellent permeability, chemical stability, and compatibility with silicate-based materials [27-29]. The effective interaction with the weathered matrix is achieved through the combination at the molecular level. TEOS-based reinforcement materials have dual functions - both deep reinforcement of the matrix and surface hydrophobic treatment can be achieved, while meeting the core requirements of maintaining historical authenticity in the protection and restoration of cultural relics. The current research focuses on optimizing the dynamic balance between penetration depth and reinforcement efficiency through controllable hydrolysis-condensation reaction to ensure the compatibility of materials with the original mineral components. Franzoni [30] et al.used TEOS to treat sintered clay bricks, and their penetration depth (about 10mm), porosity, and water absorption decreased, and compressive strength increased significantly. Liu [31] et al.used TEOS as an inorganic precursor to compound organic and inorganic materials to prepare a highly waterproof concrete surface coating. Maravelaki [32] et al added TEOS to the nano-calcium oxalate to consolidate the stone, showing interfacial compatibility and enhancing the surface hydrophobicity after treatment. Due to the application and advantages of TEOS in the protection of cultural relics, the SiO_2 aerogel synthesized on its basis has the advantages of high mechanical strength and good weather resistance, but its brittleness is strong, and its toughness is poor, and it is easy to crack when solidified [33-34]. Magnesium acrylate is composed of magnesium ions (Mg_2) and two acrylic radicals (CH_2CHCOO). It has high reactivity and can form a crosslinked polymer network through free radical polymerization [35]. Rubio-Retama

[36] et al.synthesized polyacrylic acid magnesium gel using magnesium acrylate monomer. Wei [36] introduced magnesium acrylate as the main precursor of polymer gel network to synthesize elastic plugging hydrogel. By combining silicon dioxide and magnesium acrylate, an organic-inorganic composite gel is formed, which can take advantage of the complementary characteristics of the two materials. SiO_2 provides hardness, strength, and weather resistance, and can enhance the weathering resistance and hydrolysis resistance of bricks [37]. Magnesium acrylate endows the composite with flexibility and toughness, enhances its adhesion and crack resistance, and avoids stress concentration or cracking caused by temperature changes and humidity fluctuations [38].

In this study, tetraethyl orthosilicate (TEOS) was used as a silicon source to prepare silica gel pre-polymerization solution by sol-gel method. The silica-acrylate composite gel was synthesized by mixing 25 % magnesium acrylate solution with silica pre-polymerization solution, and introducing crosslinking agent and reducing agent. The pre-polymerized liquid is injected into the brick matrix by vacuum pressure impregnation technology, so that it can fully penetrate into the interior and form a composite gel in situ. This method significantly improves the densification degree of the pore structure inside the gray brick through the synergistic effect of pore filling strengthening and particle surface modification. The chemical structure of the composites was characterized by Fourier transform infrared spectroscopy (FTIR), X-ray diffraction (XRD) and X-ray fluorescence spectroscopy (XRF). The synergistic effects on sol-gel reaction rate, network density and modification performance were quantitatively studied by three-level four-factor orthogonal experimental design. The gel time of the modified ash brick, the mass loss under three environmental conditions, the compressive strength of the ash brick, the scanning electron microscope (SEM) analysis and the durability were comprehensively evaluated, and the best ratio was obtained. In order to verify the durability of the modified brick under the action of natural external environment, the best proportion of modified gray brick is used to build the wall outdoors. The experimental results show that the modified gray brick has a significant improvement in compressive strength, durability and water resistance. Through the synergistic effect of pore consolidation and hydrophobic modification, the synthesis and internal modification process of silicon magnesium acrylate prepolymer liquid was established to inhibit the structural deterioration of ancient building ash bricks caused by dry-wet alternating cycles. The durability of bricks can be improved without replacing the original building materials. From the two aspects of protecting the original appearance and improving the function, it provides an extensible and sustainable reinforcement strategy for the protection of ancient buildings.



Fig. 1. Kaifeng city wall and Luoyang Longmen Grottoes disease

2. Experimental materials and experimental program

2.1. Experimental materials and instruments

2.1.1 Main Raw Materials

In this study, the gray brick sample was taken from the recycled building materials of traditional houses in Kaifeng ancient city. The material has high porosity and excellent water absorption characteristics, and can typically characterize the structural characteristics of historical masonry. The gray brick was processed into a 50 mm × 50 mm × 50 mm cube test block by a cutting machine, and the samples with visual color difference were removed to retain the test piece with the mean deviation of dry weight within ± 3 %. All samples were rinsed 10 times with deionized water to remove residual salts and contaminants that may interfere with the test. The mineralogical analysis of X-ray diffraction (XRD) shows that the main component of the gray brick is quartz, followed by anorthite, albite, and microcline. The specific quantitative data are shown in Table 1, and the crystallographic spectrum is shown in Fig. 2.

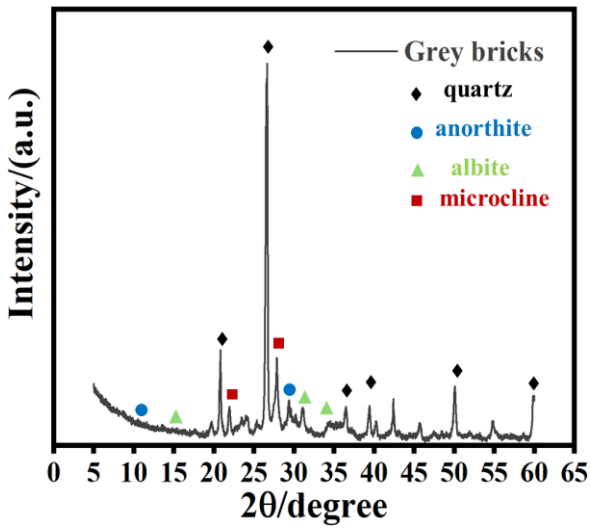


Fig. 2. XRD test of original grey brick

Table.1. The main chemical composition of grey brick

Composition	SiO_2	Al_2O_3	CaO	Fe_2O_3	K_2O	MgO	Na_2O	TiO_2
Content (%)	65.40	14.85	7.02	4.97	3.93	3.04	2.05	0.65

2.1.2. Gel main materials and synthetic equipment

The main component of the prepolymer solution are Tetraethyl orthosilicate (TEOS,99.99%),; Anhydrous ethanol (C_2H_6O), AR ; Glacial acetic acid ($C_2H_4O_2$,99.7%) ; Ammonium hydroxide ($NH_3 \cdot H_2O$,25-28%, evaporation residue ≤0.002%) ; Deionized water; Magnesium acrylate solution($C_3H_4O_2$,25%);N,N'-Methylenebisacrylamide (MBA,≥99 %, crosslinking agent); Triethanolamine (TEA, accelerator); Ammonium persulfate (APS,≥99 %, initiator).The main instruments and equipment for the Electric Heating Blast Drying Oven (Model 101-3B, Lianjing Technology Whale Control Instruments); Negative Pressure Vacuum Pump (Model 1550D, dual-head, Zhejiang Taizhou Tengyuan Co.); field emission scanning electron microscope (JEOL JSM-7610F Plus, JEOL Ltd.); X-ray diffractometer (Bruker D8 Advance); Fourier transform infrared spectrometer (Nicolet IS10, Nicolet, USA); X-ray fluorescence spectrometer (ARLAdvant X Intellipower™3600, Thermo Fisher Scientific, USA).

2.2. Preparation of specimens

2.2.1 Preparation of silica aerogels

Firstly, the quantitative ethyl orthosilicate was poured into anhydrous ethanol, and deionized water was added after the constant temperature magnetic stirrer was fully stirred. Then, the pH test pen was inserted into the solution, and the catalyst (glacial acetic acid) was slowly added dropwise. The pH value was adjusted to the range of 3-4, and the stirring time was not less than 90 minutes to ensure the hydrolysis reaction was sufficient. After stirring for 90 minutes, ammonia was added dropwise and stirred again for 60 minutes to make the condensation reaction fully form a prepolymer solution. A certain amount of 25 % magnesium acrylate solution was added to MBA (cross-linking agent), and TEA (reducing agent) was added after stirring for 30 min. After 10 min, APS (initiator) was stirred at 25 ° C water bath for 60 min.

2.2.2 Preparation of modified grey bricks

The brick sample was taken out from the blast drying box and placed in a vacuum negative pressure barrel, poured into different proportions of magnesium acrylate-silica prepolymer solution, and the intermediate vacuum negative pressure barrel was used as a safety protection device. The vacuum pump is used to gradually pump the air out of the vacuum barrel, forming a pressure difference between the inside and outside of the vacuum test tube. This horizontal pressure gradient is conducive to the perfusion of silica gel prepolymer into the pores of gray bricks under negative pressure conditions. After the negative pressure air treatment is completed, the intake valve is opened to restore the vacuum barrel to normal pressure. After the sample was taken out, the excess modifier on the surface of the brick was wiped off with a degreasing gauze.

2.3. orthogonal test design

The orthogonal experimental design (L9 matrix) of four factors and three levels was used to systematically explore the synergistic effect of solution mixing ratio (A), crosslinking agent concentration (B), reducing agent dosage (C) and initiator content (D) on the formation of gel network. As shown in Table 2, while minimizing the number of experimental iterations, the order of primary and secondary effects of each factor on the target variable is determined, and the optimal combination conditions are found.

Table.2. Silica gel orthogonal test table

Samplegroup number	Sample number	A	B	C	D	Silicon dioxide prepolymer (g)
		Solution ratio	MBA	TEA	APS	
1	$A_1B_1C_1$	80%/20%	0.5%	0.5%	1%	40
2	$A_2B_1C_1$	80%/20%	1%	1%	1.5%	40
3	$A_3B_1C_1$	80%/20%	1.5%	1.5%	2%	40
4	$A_2B_1C_2$	70%/30%	0.5%	1%	2%	35
5	$A_2B_2C_2$	70%/30%	1%	1.5%	1%	35
6	$A_2B_3C_2$	70%/30%	1.5%	0.5%	1.5%	35
7	$A_3B_3C_1$	60%/40%	0.5%	1.5%	1.5%	30
8	$A_3B_3C_2$	60%/40%	1%	0.5%	2%	30
9	$A_3B_3C_3$	60%/40%	1.5%	1%	1%	30

2.4. Testing method

2.4.1 Fourier transform infrared spectroscopy (FTIR)

The chemical structure of the composite formed by the combination of magnesium acrylate and silica gel was analyzed by Fourier transform infrared spectroscopy (FTIR). Determine the type of cross-linking between the two materials, changes in functional groups, and how to combine through chemical bonds.

2.4.2 X-ray fluorescence spectrum (XRF)

Total element analysis was performed using an X-ray fluorescence spectrometer (XRF). After the gel was dried, ground into fine powder, and less than 200 mesh, the sample was prepared by the compression method. The binding effect of the two was judged by the substances generated by the silica-magnesium acrylate composite gel.

2.4.3 X-ray Diffraction (XRD)

A wide-angle Diffraction Test was performed using X-ray Diffraction (XRD). The scanning angle range was 5 ° -60 °, and the scanning rate was 3 ° / min. It is used to analyze the composite after the combination of silica-magnesium acrylate composite gel. The crystal phase and its structure information are inferred by the change of the position and shape of the diffraction peak, and the type and structure of the substance generated after the combination of magnesium acrylate and silica gel are judged.

2.4.4 Composite gel mass loss test

Considering the volume stability of the material, the mass loss rate of the silica - magnesium acrylate composite gel was tested under three temperature control environments: room temperature (25°C), low temperature (-15°C), and high temperature (60°C), respectively, to evaluate the changes in its stability under factors such as time and temperature. The mass is measured once every 24 hours for 10 consecutive days. Calculate the mass loss rate according to Eq (1). For each group of 3 parallel samples, take the average value as the final data.

$$L = \frac{m_0 - m_1}{m_0} \quad (1)$$

Where L represents the mass loss rate; m_0 denotes the initial mass of the specimen; m_1 indicates the mass after specific treatments (low-temperature freeze-thaw cycles, ambient exposure, or high-temperature drying.

2.4.5 Test of setting time of composite *gel*

Considering that the gelation time is the key factor affecting the penetration depth, the synergistic effect of the four influencing factors on the gelation time of the composite gel was investigated by orthogonal experiments of four factors and three levels. Each group had 3 parallel samples, and the average value was the final data.

2.4.6 Compressive strength test of modified gray brick

Uniaxial compression test was carried out on the modified ash brick sample. The test method is referred to (GB / T2542-2012) "Test methods for wall bricks" [39]. At a loading speed of 0.2mm / s, the displacement control loading method was used until the sample was destroyed. Three samples were selected for each experimental group,

and the average value was obtained as the final compressive strength. The compressive strength is calculated according to Eq. (2):

$$P = \frac{F}{A} \tag{2}$$

Where P is the compressive strength of the specimen (MPa), F is the failure load of the specimen (KN), and A is the cross-sectional area of the specimen (mm^2).

2.4.7 Scanning electron microscope (SEM)

The field emission scanning electron microscope system (SEM) was used to test the gray brick and composite gel modified by silica-magnesium acrylate prepolymer liquid, and the microstructure evolution of the ash brick and composite gel modified by silica-magnesium acrylate prepolymer liquid was studied. By comparing the microstructure of the ash brick before and after modification, the penetration depth, uniformity of the composite gel, the bonding between the silica and the ash brick matrix, and the change of the pore morphology were observed.

3. Experimental results and analysis

3.1. FTIR test results

According to Ellerbrock et al [40]. Findings, the Si–O–Si network of amorphous silica may incorporate trace heteroatoms that shift characteristic infrared band positions and alter peak morphologies, distinguishing it from a purely amorphous Si phase.Fig.3 shows the FTIR spectrum, indicating that the absorption peaks at wave numbers 461.97 cm^{-1}, 674.21cm^{-1}, and 802.23 cm^{-1} belong to the symmetrical stretching vibration absorption peaks of the Si-O bond, suggesting that silica exists in the composite gel and its amorphous form is dominant. The wide peaks at 958.14 cm^{-1} and 1092.02 cm^{-1} were associated with the cross-linking reaction between silicon dioxide and magnesium acrylate, showing the formation of Si-O-Mg and Si-O-C bonds. The absorption peak at 560 cm^{-1} wave number can be attributed to the stretching vibration absorption peak of the Mg-O bond, the absorption peak at 834.28 cm^{-1} wave number belongs to the bending vibration absorption peak of the C-C and C-O single bonds, and the absorption peak at 1365 cm^{-1} wave number belongs to the symmetrical stretching vibration absorption peak of the carboxyl COO- group. The absorption peak at wave number 1438.62 cm^{-1} belongs to the C-H bending vibration peak, the absorption peak at wave number 1558.62 cm^{-1} belongs to the stretching vibration absorption peak of the alkene bond C=C, and the absorption peak at wave number 1643.09 cm^{-1} belongs to the asymmetric stretching vibration absorption peak of the carboxyl C=O double bond. The absorption peak at the wave number of 3402.97 cm^{-1} belongs to the stretching vibration absorption peak of hydroxyl OH, adsorbing water, or crystalline water.

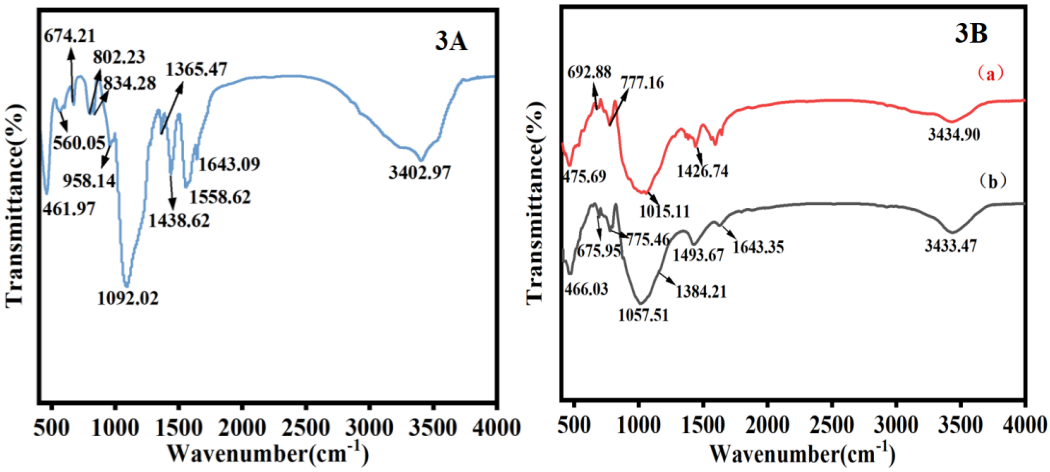


Fig.3 FTIR test results Composite gel and before and after modified grey brick

The FTIR spectra of Fig.3B(a) correspond to the unmodified gray bricks, showing the characteristic absorption peaks at 475.69 cm^{-1}, 692.88 cm^{-1}, and 777.16 cm^{-1}. These peaks belong to the bending and stretching vibrations of the Si-O-Si bond, respectively, indicating that silica exists in an amorphous form. Fig.3B(b) shows the FTIR spectrum of the modified grey brick, with new peaks emerging at 775.46 cm^{-1} and 1057.51 cm^{-1}, which are respectively related to the Si-O-Mg and Si-O-C bonds. These peaks confirmed that a cross-linking reaction occurred between magnesium acrylate and silica, demonstrating the successful synthesis and hybridization of the composite gel [41]. The characteristic absorption peaks of the acrylic group appeared in the spectrum, namely 1384.21 cm^{-1}, 1439.67 cm^{-1}, 1594.09 cm^{-1}, and 1643.35 cm^{-1}, further indicating the synthesis of the magnesium acrylate and silica composite gel inside the brick, forming C-H, C=C, and C=O bonds. Wide peaks at 3433.47 cm^{-1} and 3434.90 cm^{-1} appeared in both spectra, indicating that residual moisture or hydration might still exist, which might be related to the influence of moisture during the crosslinking process.

3.2 XRF test results

The X-ray fluorescence (XRF) results are shown in Table 3 as follows,analysis revealed that SiO_2 constitutes the primary component of the composite gel, accounting for 87.132% of the total mass. This high silica content indicates that the material possesses favorable mechanical properties, such as hardness and structural strength. Magnesium was present in the form of MgO at a concentration of 8.403%, confirming its successful incorporation into the silica network during the synthesis process. The presence of SO_3 is attributed to the decomposition of the ammonium persulfate (APS) initiator used in gel formation. Other detected oxides, including CaO, Al_2O_3, and Fe_2O_3, were present only in trace amounts and are not expected to significantly influence the physicochemical performance of the composite. These results confirm that the synthesis proceeded as designed, yielding a silica–magnesium acrylate gel with the expected elemental composition and functional characteristics.

Table 3 List of major compounds

Analyte	Calibration status	Compound formula	Concentration	Unit	Calculation method
Si	Calibrated	SiO_2	87.132	%	Calculate
Mg	Calibrated	MgO	10.403	%	Calculate
Ca	Calibrated	CaO	1.027	%	Calculate
S	Calibrated	SO_3	0.821	%	Calculate
Al	Calibrated	Al_2O_3	0.521	%	Calculate
Cl	Calibrated	Cl	0.068	%	Calculate
Fe	Calibrated	Fe_2O_3	0.017	%	Calculate
P	Calibrated	P_2O_5	0.011	%	Calculate

3.3 XRD test results

The XRD test results of the silica and magnesium acrylate composite gel before and after modification with grey bricks are shown in Fig.4. The unmodified grey bricks have peaks near 2θ=26.3°, but the intensity is relatively low, indicating that there is also a small amount of SiO_2 phase in the unmodified grey bricks, but the content is relatively small. The modified grey brick showed a very strong peak near 2θ=26.3°. This might be due to the introduction of the SiO_2 phase into the interior of the brick by the composite gel, and this peak corresponds to the crystal plane of quartz. Compared with the unmodified bricks, the modified grey bricks showed a high-strength peak near 2θ=36.3°. The peaks of the modified grey bricks are generally wider, indicating that the crystal size is smaller but the strength is higher, suggesting that the content of the crystal phase increases after modification. The strong peak of the silica and magnesium acrylate composite silicone gel near 2θ=26.3° indicates that the sample contains a large amount of SiO_2 phase, and the peak near 2θ=33.1° is the characteristic peak of magnesium acrylate. The peaks near 2θ= 36.3° and 2θ= 54.7° are related to other phases or composite structures in the composite gel [41-43].

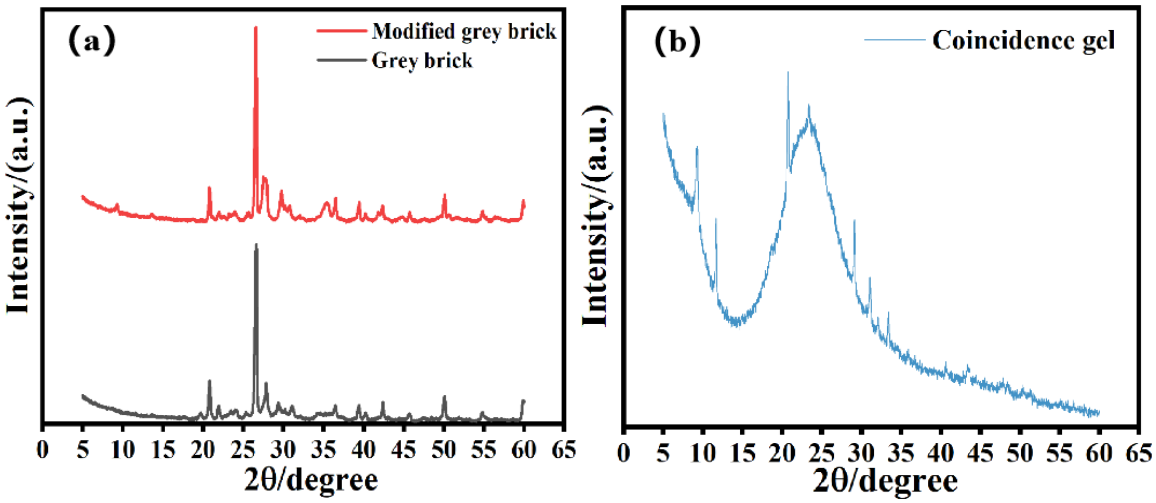


Fig.4 XRD test pattern

3.4 Solidification time of composite gel

The synergistic effect of solution ratio (A), MBA (B), TEA (C), and APS (D) on the mass loss of composite gel was quantified by orthogonal test. Taking the Solidification time of the composite gel as the evaluation standard, the polarity analysis of variance showed that RC > RA > RD > RB, and TEA were determined to be the main factor affecting the mass loss of the composite gel. The peak value was reached at the optimum conditions solution ratio 60 % / 40 %, MBA1.5 %, TEA1 %, APS1 %). Fig.5. illustrates the curing time of the composite gel, The gelation times for different formulations span 5.33–6.41 h, demonstrating a significant correlation between the penetration depth of the prepolymer solution in the grey brick matrix and modification efficiency. The extended curing time provides sufficient operation time and maximum performance for the penetration of the prepolymer in the gray brick and promotes the modification of the matrix. and optimized network maturation, thereby enhancing compressive strength and pore-sealing efficacy [44].

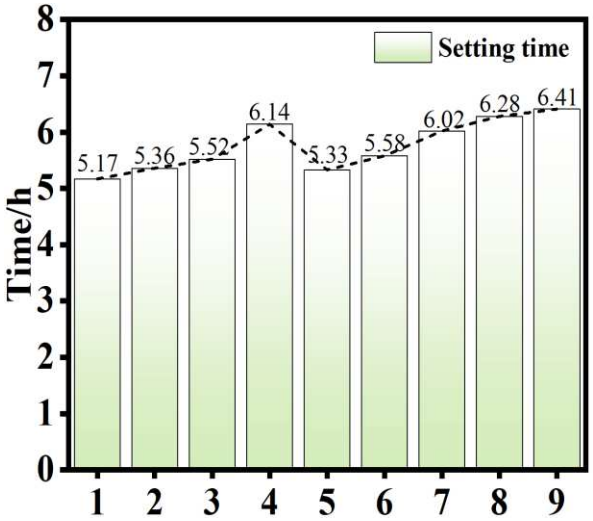


Fig. 5. Silica gel orthogonal test solidification time.

3.5. Composite gel quality loss

3.5.1 Gel quality loss at room temperature

The mass loss of the composite gel is shown in Fig.6 and Table 4. Gao et al [45]. Found that the synergistic effect of hydrogen bonds and chemical bonds can significantly improve the performance of hydrogels. We extended this concept to experimental research. The synergistic effect of solution ratio (A), MBA (B), TEA (C), and APS (D) on the mass loss of composite gel was quantified by orthogonal test. Taking the mass loss of the composite gel as the evaluation standard, the range analysis of variance showed $R_C > R_A > R_D > R_B$, and TEA was determined to be the main factor affecting the stability of the composite gel. The mass losses of each group of samples on the first day were 8.79 %, 5.17 %, 6.25 %, 7.14 %, 7.09 %, 6.69 %, 7.87 %, 7.56 % and 5.44 %, respectively. The experimental data show that the silica-magnesium acrylate composite gel exhibits a significant time-dependent mass loss behavior during the drying process at room temperature for 10 days. In the early stage, the rapid dehydration stage was observed, and the mass loss rate of all groups ranged from 5.17 % to 8.79 % on the first day. Subsequently, the dehydration rate gradually decreased, and the system reached a quasi-equilibrium state in the middle and late stages. This two-stage dehydration mode indicates the intrinsic transformation of the water transport mechanism from the initial stage dominated by surface evaporation to the later stage controlled by diffusion in the polymer network [46].

Table 4. Silica gel mass loss rate.

	$A_1B_1C_1$	$A_2B_1C_1$	$A_3B_1C_1$	$A_2B_1C_2$	$A_2B_2C_2$	$A_2B_3C_2$	$A_3B_3C_1$	$A_3B_3C_2$	$A_3B_3C_3$
1	8.79%	5.17%	6.25%	7.14%	7.09%	6.69%	7.87%	7.56%	5.44%
2	7.38%	5.06%	5.44%	6.97%	6.51%	6.49%	7.65%	6.45%	4.57%
3	5.81%	4.39%	4.71%	5.42%	6.21%	5.69%	5.62%	5.13%	3.83%
4	5.53%	4.00%	4.56%	5.15%	5.48%	5.47%	5.57%	5.02%	3.21%
5	5.50%	3.71%	4.38%	5.01%	4.98%	5.30%	5.30%	4.93%	2.40%
6	5.29%	3.42%	4.19%	4.35%	4.71%	5.19%	5.19%	4.67%	2.12%
7	3.47%	3.38%	3.85%	3.74%	4.64%	4.34%	4.34%	4.55%	1.74%
8	2.66%	3.29%	2.76%	2.61%	3.01%	3.31%	3.56%	3.89%	1.66%
9	2.41%	2.86%	2.69%	2.48%	2.93%	3.06%	2.85%	2.77%	1.58%
10	2.17%	2.01%	2.27%	2.34%	2.87%	2.79%	2.44%	2.31%	1.46%

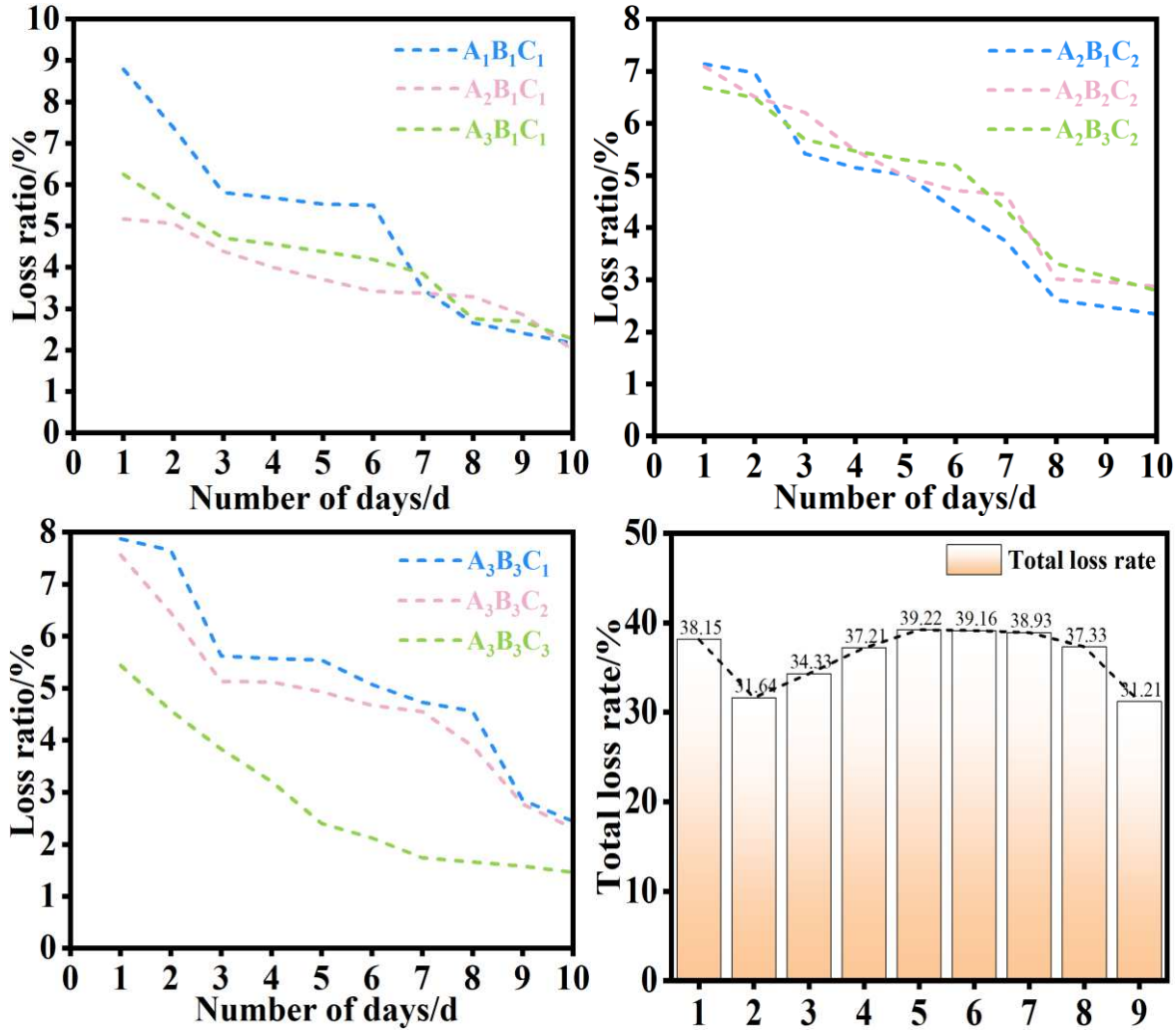


Fig.6.Gel quality loss at room temperature

3.5.2 Gel quality loss at low temperature

The synergistic effects of solution ratio (A), MBA (B), TEA (C), and APS (D) on the low-temperature mass loss of composite gel were quantified by orthogonal test. Table 5 and Fig.7 show the mass loss rate of the composite gel under different stoichiometric conditions at 15 °C during the experimental period. Taking the low-temperature mass loss of the composite gel as the evaluation standard, the order of range (R) is $R_B > R_A > R_D > R_C$, and the primary and secondary order of the four main influencing factors is: MBA, solution ratio, APS, and TEA. The mass loss rate generally showed a downward trend, which was manifested as the initial rapid consumption stage and then gradually stabilized. For the $A_1B_1C_1$ formula, the mass loss rate reached 7.53 % on the first day but decreased to 1.39 % on the 10th day, which decreased significantly with time. Under the conditions of $A_2B_2C_2$ and $A_2B_3C_2$, the significant mass loss occurred in the middle stage, indicating that these formulations were more prone to mass loss under low-temperature environmental factors. The mass loss of the $A_3B_3C_3$ formula is relatively small, and the performance is stable on the first to fifth days, and the decline rate is slow in the later period. This indicates that the stability of this composite gel with a specific stoichiometric ratio is enhanced in a low-temperature environment, and solvent retention and network consolidation are optimized.

Table 5 Gel quality loss at low temperature

	$A_1B_1C_1$	$A_2B_1C_1$	$A_3B_1C_1$	$A_2B_1C_2$	$A_2B_2C_2$	$A_2B_3C_2$	$A_3B_3C_1$	$A_3B_3C_2$	$A_3B_3C_3$
1	7.53%	7.36%	7.11%	7.77%	7.28%	6.47%	6.84%	5.43%	5.05%
2	5.82%	6.46%	6.68%	7.03%	6.16%	5.73%	6.39%	4.85%	4.17%
3	5.05%	6.12%	5.46%	6.87%	5.48%	4.41%	5.39%	4.43%	3.33%
4	4.35%	5.86%	5.33%	5.30%	4.79%	4.10%	4.92%	4.01%	2.76%
5	3.51%	4.55%	4.70%	5.15%	3.51%	3.20%	4.57%	3.56%	2.51%
6	2.10%	3.42%	3.26%	4.47%	3.31%	2.98%	3.17%	2.81%	1.85%
7	1.78%	2.87%	2.23%	3.28%	3.26%	2.86%	2.92%	2.17%	1.80%
8	1.64%	2.04%	1.43%	2.70%	1.94%	2.51%	2.57%	1.95%	1.37%
9	1.60%	1.68%	1.21%	2.62%	1.79%	1.87%	1.81%	1.58%	1.25%
10	1.39%	0.99%	1.07%	1.48%	1.66%	1.66%	1.56%	1.32%	0.85%

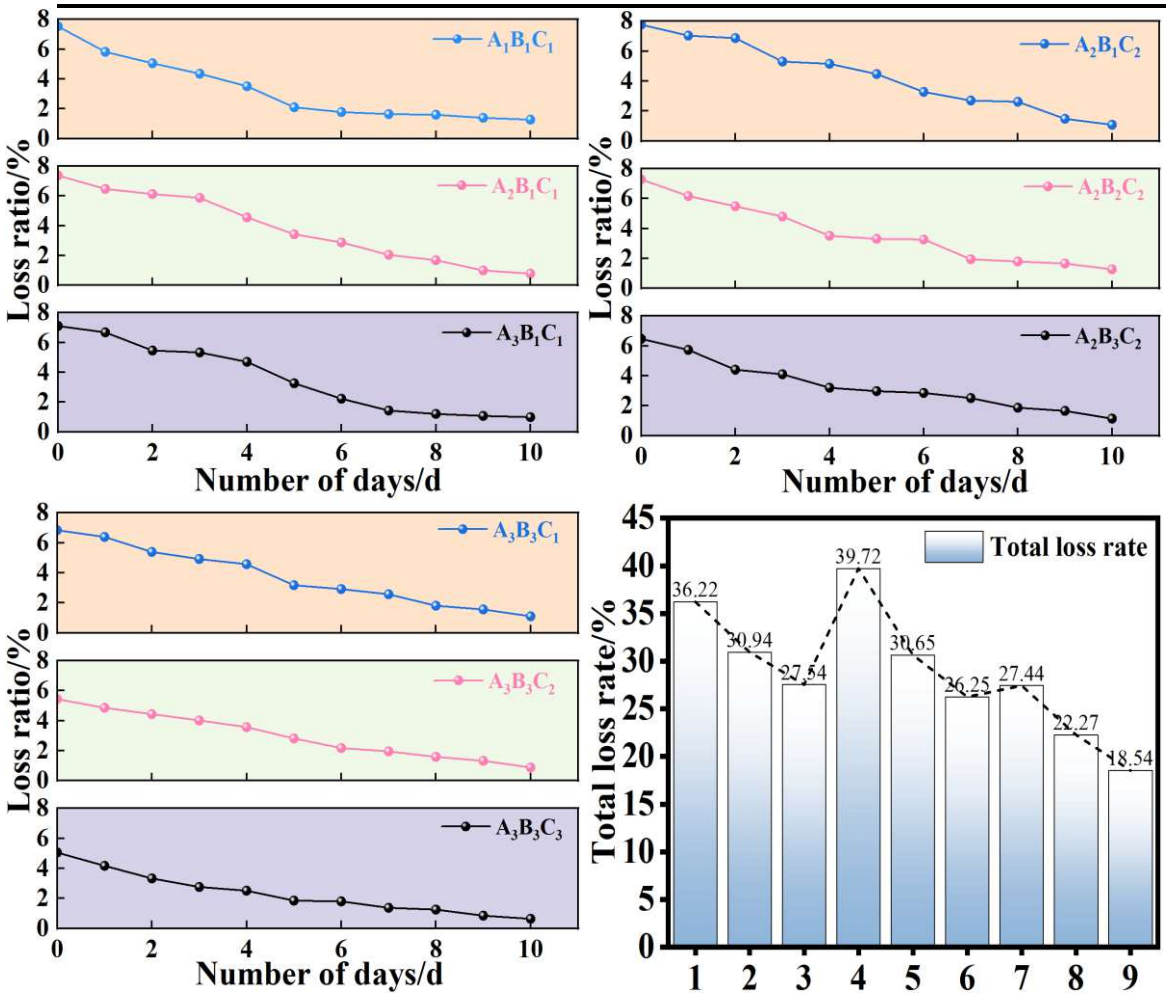


Fig.7. Composite gel loss at low temperature

3.5.3. Gel quality loss at high temperature

The synergistic effect of solution ratio (A), MBA (B), TEA (C), and APS (D) on the mass loss of composite gels at high temperatures was quantified by orthogonal test. Fig.8 and Table 6 are the mass loss rates of 10 groups of composite gels under 60 °C drying conditions. The composite gels were evaluated according to the mass loss rate at high temperatures. The range (R) was $R_A > R_B > R_C > RD$ and peaked at the optimal conditions (solution ratio 60 % / 40 %, MBA1.5 %, TEA1 %, APS1 %). In the initial dehydration stage, all samples showed an accelerated mass decay curve, reflecting the rapid evaporation of free water and the relaxation process of polymer chains. In the subsequent stabilization stage, a decrease in degradation rate was observed, indicating a dynamic balance between residual water diffusion and matrix structural integrity. The data showed that the quality loss of

$A_3B_3C_2$ and $A_3B_3C_3$ preparations was relatively stable, and the quality fluctuation was the smallest after 4 days. This indicates that in these systems, a stable balance is achieved between the diffusion of residual water molecules and the structural integrity of the matrix at high temperatures.

Table.6. Gel quality loss at high temperature

	$A_1B_1C_1$	$A_2B_1C_1$	$A_3B_1C_1$	$A_2B_1C_2$	$A_2B_2C_2$	$A_2B_3C_2$	$A_3B_3C_1$	$A_3B_3C_2$	$A_3B_3C_3$
1	13.82%	11.96%	10.73%	14.80%	15.70%	11.79%	13.94%	13.04%	10.54%
2	10.4%	9.93%	8.52%	11.27%	12.78%	9.87%	10.98%	10.71%	7.47%
3	8.21%	8.67%	6.99%	9.11%	9.29%	7.73%	8.84%	8.89%	6.41%
4	6.32%	7.01%	5.35%	7.5%	7.75%	5.97%	7.32%	6.85%	5.12%
5	5.54%	6.28%	4.67%	5.47%	5.63%	4.4%	5.79%	5.24%	4.82%
6	4.62%	5.41%	3.88%	4.62%	4.31%	3.19%	4.49%	4.02%	3.84%
7	3.81%	4.68%	2.36%	3.27%	3.76%	2.53%	3.38%	3.07%	2.71%
8	2.71%	3.81%	1.83%	2.66%	2.86%	1.59%	2.08%	2.69%	1.17%
9	1.48%	2.34%	1.55%	1.80%	1.65%	1.35%	1.53%	1.47%	0.78%
10	1.36%	1.68%	10.73%	1.54%	1.47%	1.18%	1.35%	1.33%	0.51%

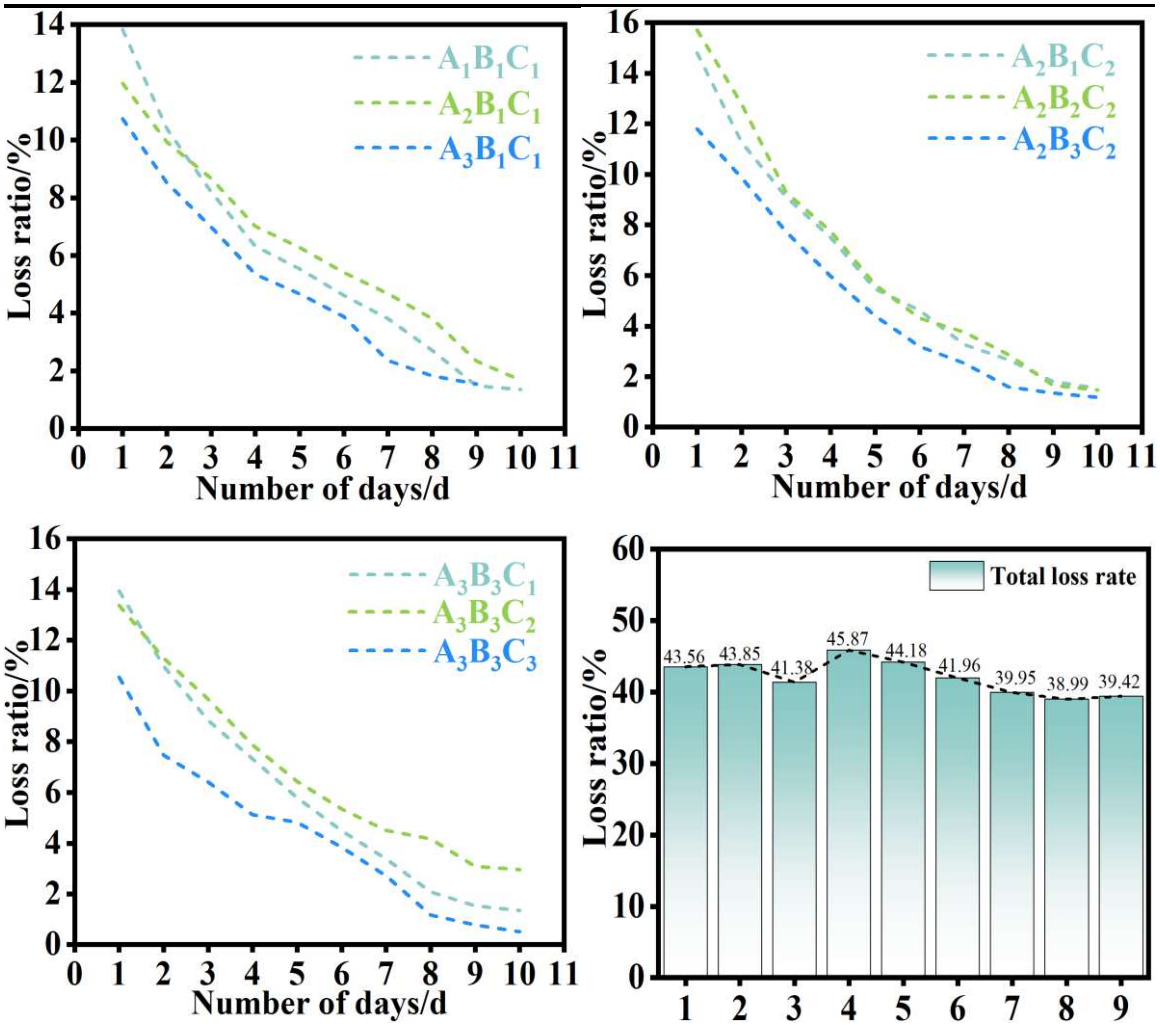


Fig.8.Gel quality loss at room temperature

3.6. Compressive strength results of modified grey brick

Building on Chandra et al [47]. plication of machine learning for predicting the compressive strength of polymer-modified bricks, we translated this predictive framework into experimental practice by systematically varying four factors in an orthogonal array. Fig.9 shows the compressive strengths of the control bricks and the modified grey bricks. Based on compressive strength as the evaluation criterion, the range values (R) were ranked as $R_A > R_B > R_D > R_C$. Under the optimum conditions (solution ratio of 70 % 30, MBA1.5 %, TEA0.5 %, APS1.5

%) reached the peak. Compared with the blank samples, all modified bricks exhibit higher compressive strengths than the unmodified ones, whose average uniaxial compressive strength is 3.31 MPa. A visual analysis reveals the following order for the compressive strengths of the modified bricks: $A_3B_3C_3$ > $A_3B_3C_1$ > $A_3B_3C_2$ > $A_2B_3C_2$ > $A_3B_1C_1$ > $A_2B_2C_2$ > $A_2B_1C_2$ > $A_2B_1C_1$ > $A_1B_1C_1$. The compressive strength of the $A_3B_3C_3$ group increases markedly, reaching 13.27 MPa-3.12 times that of the unmodified bricks. In addition, the $A_3B_3C_1$ and $A_3B_3C_2$ groups achieve compressive strengths of 10.74 MPa and 9.95 MPa, corresponding to increases of 2.52 and 2.34 times, respectively, relative to the unmodified bricks. The $A_2B_1C_1$, $A_3B_1C_1$, and $A_2B_1C_2$ groups show only modest improvements, with compressive strength increases of 0.66 MPa, 2.72 MPa, and 1.36 MPa, respectively. The remaining three experimental groups exhibit compressive strengths of 6.35 MPa, 7.87 MPa, and 7.8 MPa, respectively.

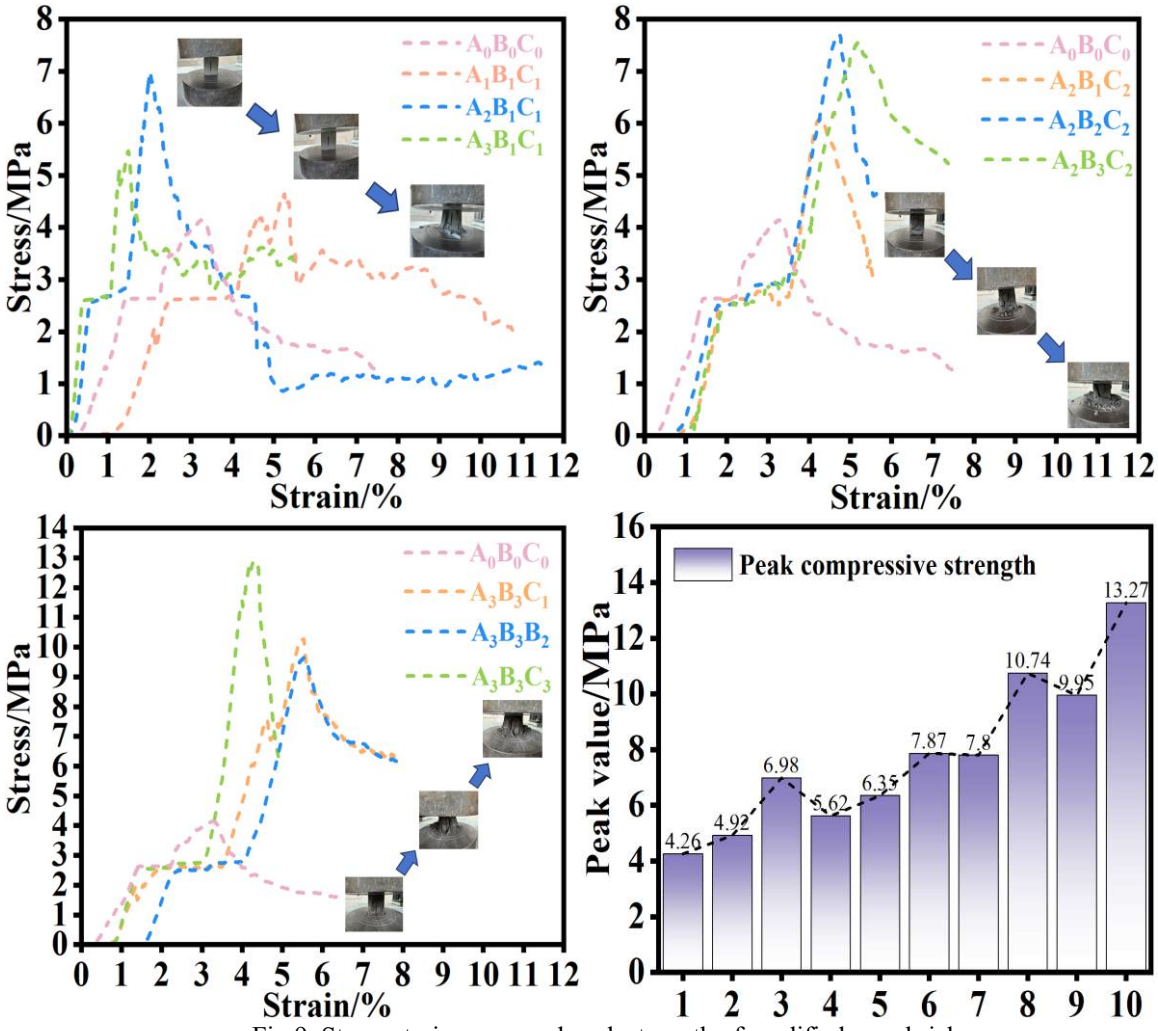
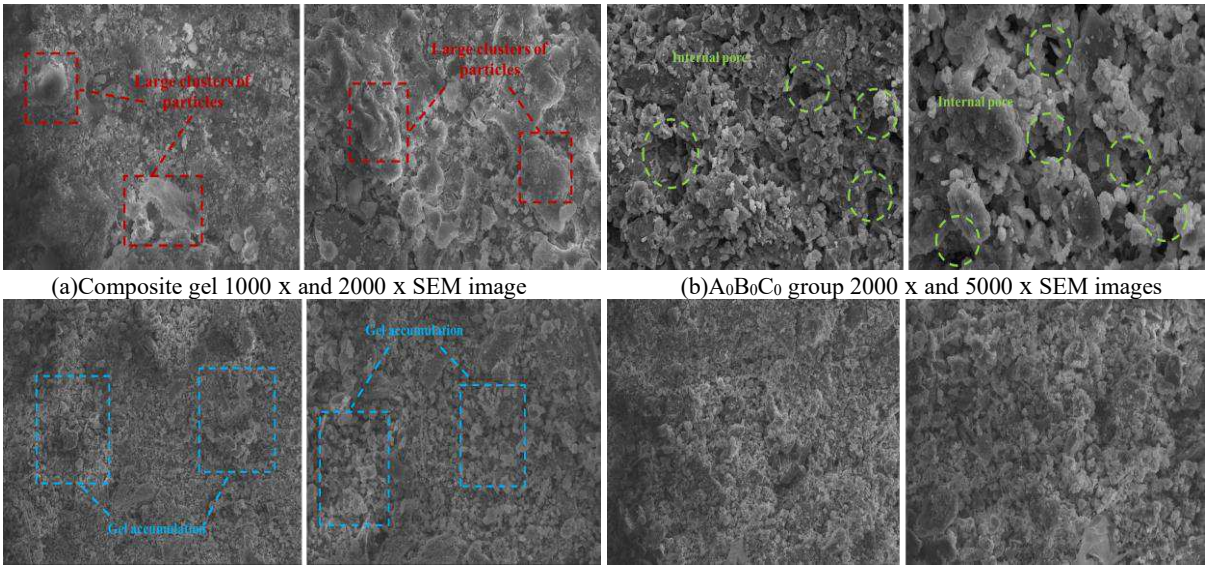


Fig.9. Stress-strain curve and peak strength of modified gray brick

3.7. SEM results

SEM was used to characterize the microstructure and morphology of the modified ash bricks. Fig.10 (a) shows the thermally cured silica-magnesium acrylate composite gel at 60 ° C, and its surface shows a uniform porous structure. The three-dimensional interpenetrating network shows obvious fractal characteristics, forming a composite material with stable structural integrity. Fig.10 (b) shows the 2000-fold and 5000-fold enlarged images of the unmodified bricks, showing the open-cell network and straight channel structure in the original matrix. These pore channels facilitate the infiltration of water and salt, thereby accelerating the degradation of the material. Fig. 10(c) shows 1000 times and 2000 times images of $A_3B_3C_2$ group modified gray bricks. The composite gel particles

are gradient distributed inside the substrate, and there are a large number of irregular particles and aggregated aggregates on the surface, indicating the agglomeration of the gel network. Fig. 10 (d) shows the 1000 times and 2000 times images of $A_3B_3C_3$ group modified ash bricks, revealing the small-scale surface irregularity and roughness in the composite gel particles. The interconnection between surface particles shows high roughness, which proves that a complex network structure is formed at the micro level. This reduction in porosity significantly enhances the overall bonding strength of the ash brick, inhibits the penetration of water and other corrosive substances, and thereby improves its corrosion resistance and weathering resistance. [48-49].



(a)Composite gel 1000 x and 2000 x SEM image (b)$A_0B_0C_0$ group 2000 x and 5000 x SEM images

(c)$A_3B_3C_2$ group 1000 x and 2000 x SEM images (d)$A_3B_3C_3$ group 1000 x and 2000 x SEM images

Fig. 10. SEM images of composite gel and partially modified grey brick

4. Outdoor durability test

The long-term alternation of complex environmental factors such as dry, wet and freeze-thaw cycles is one of the main reasons for the deterioration and durability of ancient masonry structures. The infiltration of rainwater, the rise of capillary water and the resulting hygrothermal coupling effect not only accelerate the evolution of micro-cracks and pore structure in the brick, but also significantly weaken the mechanical properties and thermal stability of the masonry[50-51]. Therefore, it is of great significance to systematically evaluate the regulation effect of modified materials on water migration and temperature response behavior of walls in real service environment, so as to reveal the mechanism of durability improvement. Compared with the indoor accelerated test, the outdoor solid wall test can more truly reflect the long-term performance of the material under the combined action of natural conditions such as rainfall, sunshine and temperature difference between day and night. . Based on this, this study constructed a multi-faceted solid test wall in the outdoor environment. Through the combination of continuous water content monitoring and infrared thermal imaging technology, the water and temperature evolution of the modified wall and the unmodified wall under different environmental conditions were compared and analyzed. Moisture content sensor is used to quantitatively characterize the spatial and temporal distribution characteristics of water in the wall, while infrared imaging is used to directly reflect the temperature field and its change trend of the wall surface in a non-contact way.

4.1 Construction and monitoring layout of the test walls

The results of orthogonal experiment showed that under the conditions of 1.5 % MBA, 1 % TEA and 1 % APS,

the ratio of ethyl orthosilicate to magnesium acrylate was 60 : 40, which was the best performance in the laboratory. In order to verify the durability of modified bricks under the action of natural external environment, this study used the above-mentioned proportion of gray bricks to modify and build four physical test walls outdoors. The length of each test wall is 1100 mm, the height is 700 mm, the thickness is 240 mm, and the geometric dimensions are consistent. Among them, No.1 and No.2 walls were modified with composite gel as the experimental group ; no.3 and No.4 walls were not treated as a blank control group. In order to more intuitively observe the water absorption and capillary water rising behavior of the wall under long-term exposure conditions, a water collection tank was set between the walls of No.2 and No.3 to collect the infiltrated water and monitor the dynamic changes of water transfer in the wall. At the same time, a variety of monitoring equipment is arranged inside or on the surface of each wall, including moisture sensor, infrared thermal imager and surface temperature and humidity recorder, etc., to monitor the moisture content change, heat and moisture transmission characteristics and water seepage path of the wall in real time. By comparing the performance differences between the experimental group and the control group under different climatic conditions, the improvement effect of the composite gel on the durability of the masonry structure can be comprehensively evaluated, which provides a scientific basis for its application in practical engineering [52]. The overall construction process and the finished appearance of the test walls are shown in Fig. 11.



Fig.11. Wall construction process and display

4.2 Moisture sensor arrangement and data acquisition

Moisture sensors were placed along the wall length direction at a height of about 30 cm from the ground on each test wall to monitor the change of moisture content inside the wall. The specific arrangement is as follows : two moisture sensors are arranged each time, and a horizontal spacing of about 70 cm is maintained between them. A total of three sets of layouts are carried out so that the sensors can cover the humidity distribution characteristics of different positions of the wall. All sensors are connected to the remote monitoring center through data lines or wireless modules to realize continuous collection, recording and real-time analysis of the moisture content inside

the wall. The monitoring system can automatically generate the curve of moisture content changing with time, and compare it with meteorological data synchronously to evaluate the influence of environmental temperature and humidity, rainfall and other factors on the moisture absorption performance of the wall. By comparing the sensor data of different walls (modified group and control group), the effect of composite gel modification on reducing the water absorption and improving the durability of the wall can be further verified. The installation and layout of the moisture sensors on the test walls are shown in Fig. 12.



Fig.12. Wall sensor installation

4.3 Infrared thermal imaging arrangement and monitoring periods

In order to systematically evaluate the thermal response behavior of modified and unmodified walls in the natural environment and its relationship with the change of water content, an infrared thermal imaging monitoring system was set up for each test wall in the outdoor test area. The infrared imager is set at about 3-5 m from the front of the wall, and the imaging height is set at about 1.2-1.5 m from the ground to ensure that the infrared field of view can completely cover the bottom to the middle and upper parts of the wall, focusing on the sensitive area of capillary water rise (0-70 cm). The monitoring focus is arranged after the end of rainfall and two typical periods of day and night in sunny days, which is used to capture the cooling characteristics of the wall under high humidity and its diurnal temperature evolution. The arrangement and field installation of the infrared thermal imaging system are shown in Fig. 13.



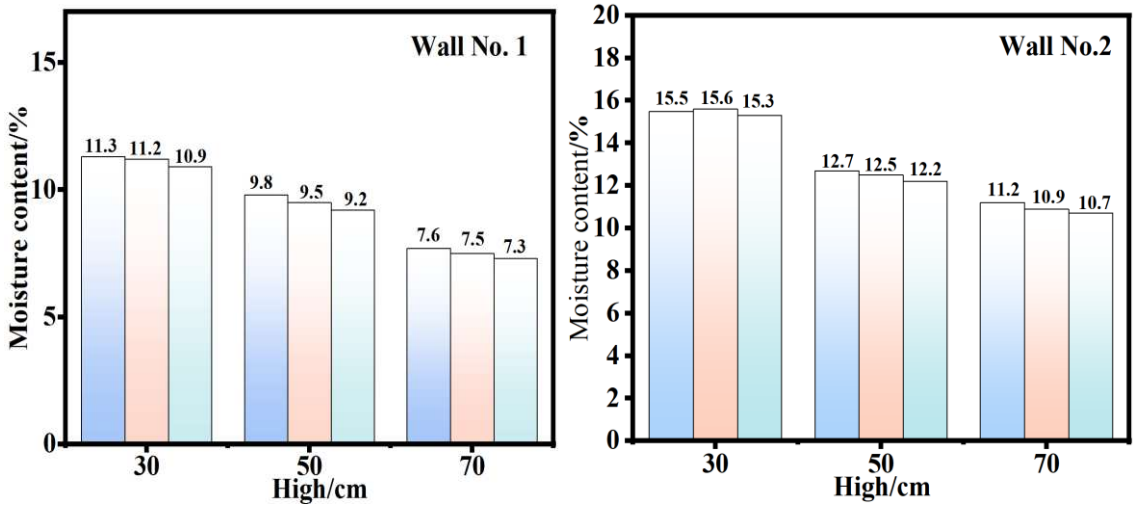
Fig.13. Infrared imaging monitoring setup

4.4 Outdoor test results

4.4.1 Sensor monitoring results

Due to the continuous rainfall process that lasted for about one month during the monitoring period, and the sinks were set at the bottom of No.2 and No.3 walls, the long-term retention of rainwater in the bottom area of the wall significantly enhanced the infiltration and accumulation of water into the interior of the wall, resulting in the

overall water content of each test wall was significantly higher than the typical level under conventional natural exposure conditions. In this context, the moisture content of the control group No.3 unmodified wall at 30 cm from the ground reached the highest value of 19.5 %, showing significant water absorption and capillary water rise characteristics. In contrast, the maximum moisture content of the No.2 modified wall, which is also affected by the catchment tank, is 15.6 % at the same height, which is about 20 % lower than that of the No.3 wall, indicating that the composite gel modification can effectively inhibit the infiltration and retention of water into the interior of the brick in an unfavorable water-bearing environment. Further analysis of the No.1 modified wall without the sink found that the maximum moisture content at the height of 30 cm was only 11.3 %, which was about 42 % lower than that of the No.3 wall in the control group, which was significantly lower than that of other test walls. It fully reflects the significant weakening effect of the composite gel on the water absorption performance of the brick. In addition, as the monitoring height increases from 30 cm to 70 cm, the water content in each wall shows a gradual downward trend, reflecting that the migration of water along the height direction is gradually attenuated by capillary action. However, compared with the control group, the water content of the modified wall decreased more significantly, indicating that the composite gel effectively limited the vertical migration process of water by closing the connected pores and weakening the continuity of the capillary channels. The above results show that the composite gel modification not only reduces the overall water content of the wall in the wet environment, but also has significant advantages in inhibiting the rise of capillary water and improving the wet migration behavior of the wall, which provides a strong support for its durability improvement in the complex natural environment[53-54]. Fig. 14 presents the variation of moisture content with monitoring time at different heights for the three test walls, which visually confirms the above comparison.



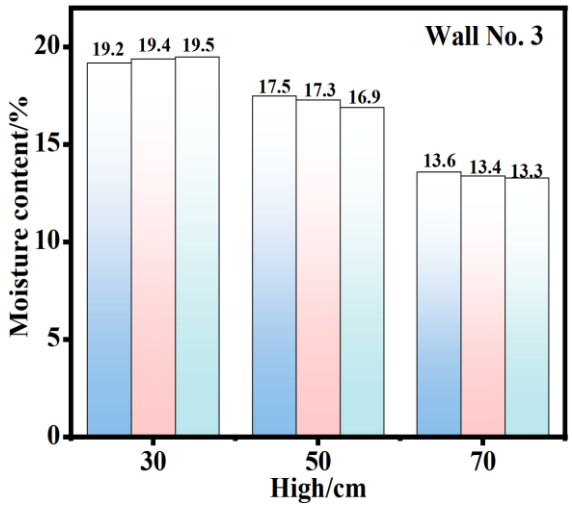
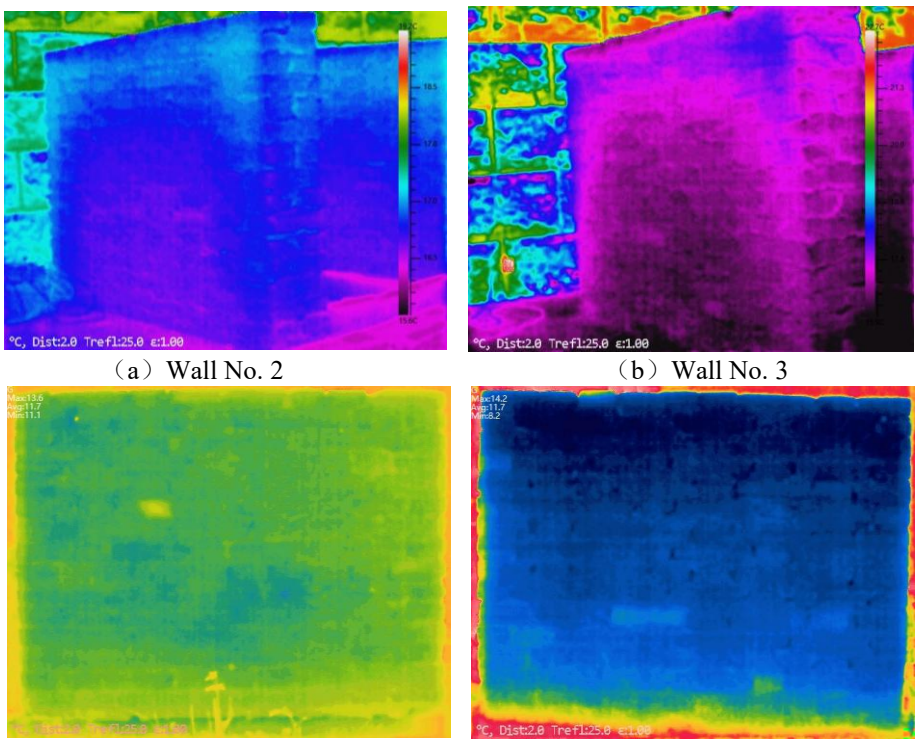


Fig. 14. Wall moisture content

4.4.2 Infrared imaging results

After the end of the rainfall process, infrared thermal imaging monitoring was carried out on each test wall to evaluate its thermal response behavior and hygrothermal coupling characteristics under high humidity environment. The results of infrared imaging showed that the unmodified wall of the control group 3 showed a significantly darker color in the thermal imaging map, corresponding to a lower surface temperature distribution. This phenomenon is highly consistent with the aforementioned water content monitoring results, indicating that rainwater is largely retained in the unmodified wall, resulting in a significant increase in the internal water content of the wall. Due to the high specific heat capacity and thermal conductivity of water, its existence enhances the heat capacity and heat dissipation capacity of the wall, which leads to the decrease of the overall temperature of the wall after rain, and shows low temperature characteristics in the infrared image. In contrast, the No.2 modified wall with the same catchment and under the same environmental conditions showed a lighter temperature color in the same period of infrared imaging, and its surface temperature was significantly higher than that of the No.3 wall. This indicates that the composite gel modification effectively weakens the infiltration and retention process of rainwater inside the wall, reduces the water content level of the wall, and thus maintains good thermal insulation performance under wet conditions. The results further verified the significant role of the composite gel in inhibiting water migration and improving the hygrothermal response of the wall from the macroscopic thermal point of view. In addition, the infrared imaging comparison of No.1 modified wall without catchment tank at different time periods showed that the temperature increased significantly under the action of solar radiation during the day, and the color of thermal imaging was significantly lighter than that at night. At night, with the enhancement of radiation heat dissipation, the surface temperature of the wall gradually decreases, and the imaging color deepens accordingly. The corresponding infrared thermal images of the three test walls at different monitoring periods are presented in Fig. 15.



（a）Wall No. 2　（b）Wall No. 3

（c）Wall No. 1　（d）Wall No. 1

Fig. 15. Infrared monitoring of the wall

4. Discussion

In this study, a new type of silicon-magnesium composite gel was synthesized by in-situ copolymerization and vacuum-assisted pressure infiltration, which significantly improved the performance of modified gray bricks. The formation of Si-O-Mg and Si-O-C covalent bonds-FTIR absorption peaks at 958 and 1092 cm-1 proved that a strong chemical bond was provided between the organic polymer network and the inorganic silica matrix. XRF analysis showed that 87.1 % of SiO_2 and 10.4 % of MgO confirmed the dominant role of silica in endowing the gel network with hardness, while magnesium acrylate helped to enhance the toughness and flexibility of the gel network [55]. The XRD results further show that the composite treatment increases the strength of the quartz phase at $2\theta = 26.3$ ° by more than 140 %, and introduces new peaks at 36.3 ° and 54.7 °, indicating that the nanocrystalline phase is formed in situ and the pore structure is refined. The diffraction peak of the modified brick is wider, indicating that the crystal size is reduced and the active phase distribution is more uniform, which is related to the observed compressive strength increased by 2.3-3.1 times compared with the untreated sample [56–60].

Orthogonal experiments show that a TEOS-to-magnesium acrylate ratio of 60:40, with 1.5% MBA, 1% TEA, and 1% APS, achieves optimal solidification time, minimal mass loss, and maximum mechanical enhancement across temperature ranges. The mixed hydrogel exhibits two-stage dehydration—rapid surface evaporation followed by diffusion-controlled internal transport—providing sufficient working time for deep penetration before setting. SEM observations confirmed a pore-filling mechanism: the composite gel forms an interpenetrating network, blocks capillaries and microcracks, reduces water absorption by 74%, and limits mass loss under 20 dry–wet or freeze–thaw cycles to ~50%, outperforming pure TEOS due to the synergy of inorganic rigidity and polymer elasticity. Molecular-level crosslinking combined with nanocrystalline phase formation enables deep reinforcement, enhancing durability and hydrophobicity.Moisture monitoring further supports these findings. During a month-long rainy period, untreated walls reached 19.5% moisture at 30 cm height, whereas modified walls peaked at

15.6%, or 11.3% without a water-collection trough—a ~42% reduction. Infrared thermography revealed that treated walls maintained warmer, more uniform temperatures and faster thermal recovery, while untreated walls appeared darker and colder. Together, these results confirm that the composite gel not only reinforces the microstructure but also improves the wall's moisture–heat performance [61–62].

Despite these achievements, the long-term performance of composite-treated bricks under field conditions remains to be verified. Future work should include accelerated weathering tests under UV irradiation and acidic environments, as well as monitoring potential changes in permeability, and compatibility with historical materials.

5. Conclusions

In this study, a new type of silicon-magnesium composite gel was synthesized through in-situ copolymerization and vacuum-assisted pressure infiltration methods to modify the gray bricks, thereby improving their mechanical properties. Through orthogonal experimental design, various performance tests were conducted, including gelation time, mass loss experiments, compressive strength of the modified gray bricks, durability in outdoor environments and temperature influence, and scanning electron microscope analysis. Through the discussion and comparison of the experimental results, the following conclusions were drawn:

(1) FTIR spectra showed the characteristic absorption at 958 and 1092 cm-1, confirming the covalent bonds of Si-O-Mg and Si-O-C. XRF measured 97.54 wt % SiO2 / MgO in the gel, while XRD found new amorphous crystal peaks at 36.3 ° and 54.7 °. The quartz strength increased by 142 % at 26.3 ° and widened at 20.8 °, indicating network densification and grain size reduction.

(2) Through the comparison and analysis of orthogonal experiments, the best ratio (solution ratio 60%/40%, MBA1.5 %, TEA1 %, APS1 %) was obtained. Under the optimum conditions, the solidification time is 6.41 h, the mass loss is less than 50 % in three different environments, and the compressive strength is increased by 3.21 times. The moisture content monitoring and infrared thermal imaging both indicate that the composite gel treatment significantly inhibits water penetration of the wall, reduces capillary rise, and improves thermal stability and temperature uniformity.

(3) SEM observation confirmed the pore-filling mechanism, and the gel formed an interpenetrating network, blocking capillary channels and microcracks. Effectively reduce the migration path of water.

(4) The composite gel modification significantly reduced the moisture content of the wall under continuous rainfall conditions, effectively inhibited the water penetration and capillary water rise, reduced the diurnal temperature fluctuation, and significantly improved the thermal stability. The consistent results of moisture content monitoring and infrared imaging show that the composite gel modification can significantly improve the hygrothermal coupling performance of the wall, thereby improving its durability in complex natural environments.

(5) Improve the durability of bricks without replacing the original building materials. From the two aspects of protecting the original appearance and improving the function, it provides an extensible and sustainable reinforcement strategy for the protection of ancient buildings.

Declaration of Competing Interest

The authors declare that they have no known competing financial interests or personal relationships that could have appeared to influence the work reported in this paper.

Data and code availability

The datasets used or analysed during the current study are available from the corresponding author on reasonable request.

Acknowledgements

We gratefully acknowledge the financial support from the Key Research and Development Special Project of Henan Province in the Year 2023 (Grant 231111321100), The National Natural Science Foundation of China (Grant 12302149).

Author contributions

Tingting Yue: Writing – original draft, Writing – review & editing, Conceptualization, Project administration, Software, Validation. **Jianwei Yue:** Conceptualization, Funding acquisition, Supervision.

References

[1] Shen Y, Yan X, Yu P, et al. Seismic resistance of timber frames with mud and stone infill walls in a Chinese traditional village dwelling[J]. Buildings, 2021, 11(12): 580. https://doi.org/10.3390/buildings11120580.

[2] Abdalla A A, Mohammed A S, Rafiq S, et al. Microstructure, chemical compositions, and soft computing models to evaluate the influence of silicon dioxide and calcium oxide on the compressive strength of cement mortar modified with cement kiln dust[J]. Construction and Building Materials, 2022, 341: 127668. https://doi.org/10.1016/j.conbuildmat.2022.127668

[3] Doni M, Fierascu I, Fierascu R C. Recent developments in materials science for the conservation and restoration of historic artifacts [J]. Applied Sciences, 2024, 14(23): 11363. https://doi.org/10.3390/app142311363

[4] Maucourant C, O'Flaherty F, Drago A. Applicability and efficacy of an enhanced nanolime consolidation technique for British Museum limestone objects[J]. Journal of Cultural Heritage, 2023, 62: 339-348. https://doi.org/10.1016/j.culher.2023.04.007

[5] Gomez-Villalba L S, Salcines C, Fort R. Application of inorganic nanomaterials in cultural heritage conservation, risk of toxicity, and preventive measures[J]. Nanomaterials, 2023, 13(9): 1454.https://doi.org/10.3390/nano13091454

[6] Wang K, Xu G, Li S, et al. Geo-environmental characteristics of weathering deterioration of red sandstone relics: a case study in Tongtianyan Grottoes, Southern China[J]. Bulletin of Engineering Geology and the Environment, 2018, 77: 1515-1527. https://doi.org/10.1007/s10064-017-1128-y.

[7] Abdalla A, Salih A. Microstructure and chemical characterizations with soft computing models to evaluate the influence of calcium oxide and silicon dioxide in the fly ash and cement kiln dust on the compressive strength of cement mortar[J]. Resources, Conservation & Recycling Advances, 2022, 15: 200090. https://doi.org/10.1016/j.rcradv.2022.200090 .

[8] Patil S M, Kasthurba A K, Patil M V. Characterization and assessment of stone deterioration on Heritage Buildings[J]. Case Studies in Construction Materials, 2021, 15: e00696. https://doi.org/10.1016/j.cscm.2021.e00696.

[9] Zhang T, Xia C, Ma Y, et al. Effects of tree density variations on outdoor heritage conservation: Numerical study of an ancient brick city wall with four orientations[J]. Building and Environment, 2024, 254: 111392. https://doi.org/10.1016/j.buildenv.2024.111392.

[10] Timoncini A, Brattich E, Bernardi E, et al. Safeguarding outdoor cultural heritage materials in an ever-changing troposphere: Challenges and new guidelines for artificial ageing test[J]. Journal of Cultural Heritage, 2023, 59: 190-201. https://doi.org/10.1016/j.culher.2022.12.003.

[11] Sennakesavan G, Mostakhdemin M, Dkhar L K, et al. Acrylic acid/acrylamide based hydrogels and its properties-A review[J]. Polymer Degradation and Stability, 2020, 180: 109308.https://doi.org/10.1016/j.polymdegradstab.2020.109308

[12] Hofheinz A, Walker R, Purcell C E, et al. The hygrothermal properties of historic bricks: Case study of traditional brick construction material in Ireland[J]. Building and Environment, 2025, 270: 112491. https://doi.org/10.1016/j.buildenv.2024.112491.

[13] Luo C, Yu Y, Zhang J, et al. Study of Heat–Mass Transfer and Salt–Frost Expansion Mechanism of Sulfate Saline Soil during the Unidirectional Freezing Process[J]. International Journal of Geomechanics, 2024, 24(10): 04024227. https://doi.org/10.1061/IJGNAI.GMENG-9.

[14] Xiao H, Zhou Z, Zhang X, et al. Soil remediation by co-disposal in sintered brick kilns: Migration characteristics of heavy metals in bricks and the kiln[J]. Waste Management, 2025, 194: 55-63. https://doi.org/10.1016/j.wasman.2025.01.006.

[15] Hao Y, Yao Z, Wu R, et al. Damage and restoration technology of historic buildings of brick and wood structures: a review[J]. Heritage Science, 2024, 12(1): 301. https://doi.org/10.1186/s40494-024-01422-y.

[16] Soulios V, de Place Hansen E J, Peuhkuri R, et al. Durability of the hydrophobic treatment on brick and mortar[J]. Building and Environment, 2021, 201: 107994. https://doi.org/10.1016/j.buildenv.2021.107994.

[17] Yin B, Fan F, Hua X, et al. Reinforced anticorrosive composite coating with mesh-brick structures and excellent air permeability on concrete[J]. Journal of Building Engineering, 2023, 76: 107378. https://doi.org/10.1016/j.jobe.2023.107378.

[18] Li Q, Wang Z, Guo H, et al. A perspective view of salt crystallization from solution in porous media: morphology, mechanism, and salt efflorescence[J]. Scientific Reports, 2024, 14(1): 23510. https://doi.org/10.1038/s41598-024-74645-5.

[19] Detho A, Kadir A A, Shayuti A, et al. Improvement of engineering properties and environmental impact of fired clay bricks utilizing industry sludge waste[J]. Scientific Reports, 2025, 15(1): 4820. https://doi.org/10.1038/s41598-025-89147-1.

[20] Abbas S, Saleem M A, Kazmi S M S, et al. Production of sustainable clay bricks using waste fly ash: Mechanical and durability properties[J]. Journal of Building Engineering, 2017, 14: 7-14.https://doi.org/10.1016/j.jobe.2017.09.008.

[21] Kazmi S M S, Munir M J, Patnaikuni I, et al. Thermal performance enhancement of eco-friendly bricks incorporating agro-wastes[J]. Energy and Buildings, 2018, 158: 1117-1129. https://doi.org/10.1016/j.enbuild.2017.10.056.

[22] Guo S, Yan J, Chen W, et al. Conservation of the weathering bricks in historical buildings using the alcoholic solution of barium hydroxide[J]. Construction and Building Materials, 2024, 452: 138887. https://doi.org/10.1016/j.conbuildmat.2024.138887.

[23] Bu N, Ye M, Wang K, et al. Fluorinated B-72 hybrid silver doped modified nanoparticle as a coating for biological corrosion protection of ancient bricks[J]. Surface and Coatings Technology, 2024, 494: 131411. https://doi.org/10.1016/j.surfcoat.2024.131411.

[24] Reyes-Tesillo B G, Hernández-Padrón G, Ferrer-Pérez J A, et al. Hybrid coating prepared with PMMA/Ti-O-Si tested under vacuum conditions for use in nanosatellites[J]. PloS one, 2025, 20(1): e0313785. https://doi.org/10.1371/journal.pone.0313785.

[25] Graziani L, D'Orazio M. Biofouling prevention of ancient brick surfaces by TiO2-based nano-coatings[J]. Coatings, 2015, 5(3): 357-365. https://doi.org/10.3390/coatings5030357.

[26] Pagliolico S L, Ozzello E D, Sassi G, et al. Characterization of a hybrid nano-silica waterborne polyurethane coating for clay bricks[J]. Journal of Coatings Technology and Research, 2016, 13: 267-276. https://doi.org/10.1007/s11998-015-9758-0.

[27] Luo Y, Xiao L, Zhang X. Characterization of TEOS/PDMS/HA nanocomposites for application as consolidant/hydrophobic products on sandstones[J]. Journal of Cultural Heritage, 2015, 16(4): 470-478. https://doi.org/10.1016/j.culher.2014.08.002

[28] Ksinopoulou E, Dragatogiannis D, Bakolas A, et al. Physical and mechanical characteristics of TEOS-modified nanocomposites[J]. Journal of Polymer Research, 2022, 29(5): 196. https://doi.org/10.1007/s10965-022-03053-y.

[29] Akhter F, Soni H L, Jamali A R, et al. Efficient adsorption of lead (II) ions from artificial wastewater by organically tailored vs TEOS-doped silica aerogels: synthesis, characterization and isotherm studies[J]. Water, Air, & Soil Pollution, 2023, 234(3): 180. https://doi.org/10.1007/s11270-023-06204-z

[30] Franzoni E, Pigino B, Leemann A, et al. Use of TEOS for fired-clay bricks consolidation[J]. Materials and structures, 2014, 47: 1175-1184. https://doi.org/10.1617/s11527-013-0120-7

[31] Liu Y, Lin Q, Chen J, et al. PDMS-OH and nano-SiO_2 Modified KH570-TEOS silica-sol coating and protective effect on concrete[J]. Colloids and Surfaces A: Physicochemical and Engineering Aspects, 2022, 648: 129279. https://doi.org/10.1016/j.colsurfa.2022.129279

[32] Maravelaki P N, Kapetanaki K, Stefanakis D. TEOS-PDMS-Calcium Oxalate Hydrophobic Nanocomposite for Protection and Stone Consolidation[J]. Heritage, 2021, 4(4): 4068-4075. https://doi.org/10.3390/heritage4040224.

[33] Wu Q, Yao R, Guo D, et al. Dual hydrophilic/hydrophobic SiO2 transparent super-hydrophobic coating with good interfacial adhesion and high mechanical robustness[J]. Journal of Materials Science, 2024: 1-16. https://doi.org/10.1007/s10853-024-10470-5

[34] Steinerová D, Kalendová A, Machotová J, et al. Environmentally friendly water-based self-crosslinking acrylate dispersion containing magnesium nanoparticles and their films exhibiting antimicrobial properties[J]. Coatings, 2020, 10(4): 340. https://doi.org/10.3390/coatings10040340.

[35] Rubio-Retama J, Tamimi F M, Heinrich M, et al. Synthesis and characterization of poly (magnesium acrylate) microgels[J]. Langmuir, 2007, 23(16): 8538-8543. 10.1021/la700696h.

[36] Wei D, Zhu K, Li H, et al. Fabrication of high-performance acrylate grouting materials from tailor made magnesium acrylate solutions[J]. Journal of Applied Polymer Science, 2024, 141(21): e55405. https://doi.org/10.1002/app.55405.

[37] AlTawaiha H, Alhomaidat F, Eljufout T. A review of the effect of nano-silica on the mechanical and durability properties of cementitious composites[J]. Infrastructures, 2023, 8(9): 132. https://doi.org/10.3390/infrastructures8090132.

[38] Saberi A, Bakhsheshi-Rad H R, Abazari S, et al. A comprehensive review on surface modifications of biode

gradable magnesium-based implant alloy: Polymer coatings opportunities and challenges[J]. Coatings, 2021, 11(7): 747. https://doi.org/10.3390/coatings11070747.

[39] GB/T 2542-2012. Test method for wall bricks [S].null,2012.12.31

[40] Ellerbrock R, Stein M, Schaller J. Comparing amorphous silica, short-range-ordered silicates and silicic acid species by FTIR[J]. Scientific Reports, 2022, 12(1): 11708. https://doi.org/10.1038/s41598-022-15882-4

[41] Panahi P, Khorasani S N, Koochaki M S, et al. Synthesis of Cloisite 30B-acrylamide/acrylic acid nanogel composite for self-healing purposes[J]. Applied Clay Science, 2021, 210: 106174. https://doi.org/10.1016/j.clay.2021.106174.

[42] Shafieyan R, Khorasani S N, Neisiany R E, et al. Synthesis and swelling behavior of the acrylamide/acrylic acid-Cloisite 30B nanocomposite gel[J]. Materials Chemistry and Physics, 2025, 333: 130382. https://doi.org/10.1016/j.matchemphys.2025.130382.4.

[43] Xu X, Liu Y, Fu W, et al. Poly (N-isopropylacrylamide)-based thermoresponsive composite hydrogels for biomedical applications[J]. Polymers, 2020, 12(3): 580. https://doi.org/10.3390/polym12030580

[44] Solyman W S E, Nagiub H M, Alian N A, et al. Synthesis and characterization of phenol/formaldehyde nanocomposites: Studying the effect of incorporating reactive rubber nanoparticles or Cloisite-30B nanoclay on the mechanical properties, morphology and thermal stability[J]. Journal of Radiation Research and Applied Sciences, 2017, 10(1): 72-79. https://doi.org/10.1016/j.jrras.2016.12.003

[45] Gao L, Luo H, Wang Q, et al. Synergistic effect of hydrogen bonds and chemical bonds to construct a starch-based water-absorbing/retaining hydrogel composite reinforced with cellulose and poly (ethylene glycol) [J]. ACS omega, 2021, 6(50): 35039-35049. https://doi.org/10.1021/acsomega.1c05614

[46] Sun N, Ji R, Zhang F, et al. Structural evolution in poly (acrylic-co-acrylamide) pH-responsive hydrogels by low-field NMR[J]. Materials Today Communications, 2020, 22: 100748. https://doi.org/10.1016/j.mtcomm.2019.100748.

[47] Chandra S S, Kumar R, Arjunasamy A, et al. Predicting the compressive strength of polymer-infused bricks : A machine learning approach with SHAP interpretability[J]. Scientific Reports, 2025, 15(1): 8090. https://doi.org/10.1038/s41598-025-89606-9

[48] Xu F, Zeng W, Li D. Recent advance in alkoxysilane-based consolidants for stone[J]. Progress in organic coatings, 2019, 127: 45-54. https://doi.org/10.1016/j.porgcoat.2018.11.003.

[49] Salazar-Hernández C, Puy-Alquiza M J, Miranda-Avilés R, et al. Comparative study of TEOS-consolidants for adobe building conservation[J]. Journal of Sol-Gel Science and Technology, 2021, 97: 685-696. https://doi.org/10.1007/s10971-020-05461-2

[50] Zheng D, Liu C, Zhang X, et al. Combined effects of solution environment and freeze-thaw cycling on the crack propagation characteristics in sandstone during loading[J]. Cold Regions Science and Technology, 2024, 217: 104014. https://doi.org/10.1016/j.coldregions.2023.104014

[51] Dong W, Wang J. Research on capillary water absorption characteristics of aeolian sand concrete under sulfate freeze-thaw coupling based on fractal theory[J]. Construction and Building Materials, 2024, 455: 139184. https://doi.org/10.1016/j.conbuildmat.2024.139184.

[52] Zhu X, Wang D, Zhang Y, et al. Study on sulfate diffusion test and mathematical model of manufactured sand concrete under typical freeze-thaw environment in Northwest China[J]. Construction and Building Materials, 2024, 419: 135559. https://doi.org/10.1016/j.conbuildmat.2024.135559.

[53] Pu C, Gao X, Wu Z, et al. Metal-silicate partitioning of Si, O, and Mg at high pressures and high temperatures: Implications to the compositional evolution of core-forming metallic melts[J]. Geochemistry, Geophysics, Geosystems, 2025, 26(2): e2024GC011940. https://doi.org/10.1029/2024GC011940.

[54] Khan S A, Khan S B, Khan L U, et al. Fourier transform infrared spectroscopy: fundamentals and application in functional groups and nanomaterials characterization[J]. Handbook of materials characterization, 2018: 317-344 .https://doi.org/10.1007/978-3-319-92955-2_9

[55] Lenhardt K R, Breitzke H, Buntkowsky G, et al. Synthesis of short-range ordered aluminosilicates at ambient conditions[J]. Scientific reports, 2021, 11(1): 4207. https://doi.org/10.1038/s41598-021-83643-w

[56] Hafez A I, Khedr M M A, Osman R M, et al. A comparative investigation of the unit cost for the preparation of modified sand and clay bricks from rice husk waste[J]. Journal of Building Engineering, 2020, 32: 101765. https://doi.org/10.1016/j.jobe.2020.101765.

[57] Roskosz M, Toplis M J, Besson P, et al. Nucleation mechanisms: A crystal-chemical investigation of phases forming in highly supercooled aluminosilicate liquids[J]. Journal of Non-Crystalline Solids, 2005, 351(14-15): 1266-1282. https://doi.org/10.1016/j.jnoncrysol.2005.02.021.

[58] Ren H S, Liu D, Tang H B, et al. Microstructure and mechanical properties of a graded structural material[J]. Materials Science and Engineering: A, 2014, 611: 362-369. https://doi.org/10.1016/j.msea.2014.06.016

[59] Kaur H, Chaudhary S, Kaur H, et al. Hydrolysis and condensation of tetraethyl orthosilicate at the air–aqueous interface: implications for silica nanoparticle formation[J]. ACS applied nano materials, 2021, 5(1): 411-422, https://pubs.acs.org/doi/10.1021/acsanm.1c03250.

[60] Guo F, Yin H, Luo H, et al. Preparation of TEOS coated responsive nanocapsules endows the coating excellent anti-corrosion properties[J]. Progress in Organic Coatings, 2024, 196: 108695,https://doi.org/10.1016/j.porgcoat.2024.108695.

[61] Rippa M, Vigorito M R, Russo M R, et al. Active Thermography for Non-invasive Inspection of Wall Painting: Novel Approach Based on Thermal Recovery Maps[J]. Journal of Nondestructive Evaluation, 2023, 42(3): 63. https://doi.org/10.1007/s10921-023-00972-8.

[62] Aversa P, Palumbo D, Donatelli A, et al. Infrared thermography for the investigation of dynamic thermal behaviour of opaque building elements: Comparison between empty and filled with hemp fibres prototype walls[J]. Energy and Buildings, 2017, 152: 264-272. https://doi.org/10.1016/j.enbuild.2017.07.055.